Additive Manufacturing 58 (2022) 103057

Contents lists available at ScienceDirect

Additive Manufacturing

journal homepage: www.elsevier.com/locate/addma

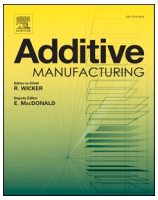

Interparticle bonding and interfacial nanocrystallization mechanisms in additively manufactured bulk metallic glass fabricated by cold spray

Ningsong Fan [a], Chunjie Huang [b], Zhongyu Wang [a], Pengfei Yu [a], Wen Chen [c], Rocco Lupoi [a], Qingge Xie [d,*], Lin Liu [e,*], Shuo Yin [a,*]

[a] Department of Mechanical, Manufacturing & Biomedical Engineering, Parsons Building, Trinity College Dublin, The University of Dublin, Dublin 2, Ireland
[b] Institute of Materials Technology, Helmut-Schmidt-University/University of the Federal Armed Forces Hamburg, Hamburg 22043, Germany
[c] Department of Mechanical and Industrial Engineering, University of Massachusetts, Amherst, MA 01003, United States
[d] Collaborative Innovation Center of Steel Technology, University of Science and Technology Beijing, Beijing 100083, China
[e] State Key Laboratory of Materials Processing and Die & Mould Technology, School of Materials Science and Engineering, Huazhong University of Science and Technology, Wuhan 430074, China

ARTICLE INFO

Keywords:
Cold spray
Additive manufacturing
Bulk metallic glass (BMG)
Bonding mechanism
Nanocrystallization

ABSTRACT

Amorphous Zr-based bulk metallic glass deposit was produced by cold spray additive manufacturing. The bonding mechanism of metallic glass particles was systematically investigated through studying the deformation behavior of individual particles after deposition. We revealed two collective particle bonding mechanisms that contributed to the formation of metallic glass deposits, i.e., high-velocity impact induced localized metallurgical bonding at the fringe of the interface, and high particle temperature induced viscosity reduction and the resultant annular metallurgical bonding band. Moreover, the dynamic evolution mechanism of the amorphous phase into nanocrystal structures at severely deformed interfacial regions during cold spray was carefully investigated. For the first time, we observed different amorphous/nanocrystal structures in cold sprayed metallic glass deposits, which can represent different evolution stages in nanocrystallization process. Based on the observation, it is inferred that the nanocrystallization process can be divided into following three stages: composition segregation, the formation of ordered 1D and 2D transition structures, and 3D nanocrystals. The current study provides new insights into the bonding mechanisms and the mechanistic nanocrystallization origins in cold sprayed bulk metallic glass deposits.

1. Introduction

Bulk metallic glasses (BMGs) are a type of multi-component amorphous alloy with unique long-range disordered but short-range ordered atomic scale structures. The amorphous structure results in the absence of crystalline defects, such as grain boundaries, dislocations, and stacking faults, leading to superior mechanical properties (e.g., high strength, high hardness and high elastic limit), exceptional soft magnetic properties, and excellent wear- and corrosion-resistance at room temperature [1–3]. Unlike traditional metallic glasses, which are fabricated through rapid solidification of molten liquids at a high cooling rate of 10^4~10^6 K/s to bypass crystallization, BMGs can be produced at lower critical cooling rates (typically less than 10^3 K/s) with a thickness of more than 1 millimeter [4]. In recent decades, BMGs have been explored by different additive manufacturing techniques, mainly including laser-based processes (e.g., laser foil printing [5], laser cladding [6], laser solid forming [7], and selective laser melting [8]) as well as thermal spray processes (e.g., high velocity oxygen/air fuel [9,10], plasma spray [11], and arc spray [12]). These additive manufacturing routes allow the fabrication of BMGs and have attracted attentions from both scientific and industrial communities. However, the complicated thermal history associated with these fusion-based processes usually leads to detrimental metallurgical defects (e.g., phase transformation, oxidation, and crystallization) that deteriorate the mechanical properties of BMGs [13].

Cold spray is a burgeoning material deposition and solid-state additive manufacturing technology, which provides an attractive alternative to produce BMGs. In this process, micro-sized particles are accelerated by heated and pressurized gas (e.g., nitrogen or helium) to high velocities (300–1200 m/s) through a de-Laval nozzle, and then the

* Corresponding authors.
E-mail addresses: qingge.xie@ustb.edu.cn (Q. Xie), lliu2000@mail.hust.edu.cn (L. Liu), yins@tcd.ie (S. Yin).

https://doi.org/10.1016/j.addma.2022.103057
Received 25 April 2022; Received in revised form 21 July 2022; Accepted 22 July 2022
Available online 23 July 2022

particles impact onto a substrate or previously deposited layers. The high kinetic energy causes rapid and severe plastic deformation of particles upon impact, which allows the consolidation of particles to deposit layer-by-layer at temperatures well below their melting points [14]. The low temperature deposition characterization of cold spray helps to minimize thermal influences, and thereby a high extent of amorphous structure is expected to be retained in BMG deposits. In cold spray, the extensive plastic deformation of spraying materials is expected to achieve dense deposits with good interparticle bonding. The plastic deformation behavior of metallic glasses highly depends on temperature and strain rate, and can be categorized into inhomogeneous deformation and homogeneous deformation [15]. Metallic glasses experience inhomogeneous deformation at low temperatures and high strain rates, which can be characterized by linear elastic behavior followed by severe localized plastic flow concentrated within thin shear bands, and the consequent catastrophic fracture. In contrast, homogeneous deformation of metallic glasses refers to the uniform deformation at a macroscopic scale, and generally takes place at higher temperatures (typically in or near supercooled liquid region, which is defined as the temperature interval between glass transition temperature (T_g) and crystallization temperature (T_x)) or lower strain rates. Furthermore, it features a transition from Newtonian flow to non-Newtonian flow with increasing strain rates. In supercooled liquid region, metallic glasses generally exhibit distinct viscous flow and superplastic deformation characteristics. The excellent processability of metallic glasses in supercooled liquid region allows net-shape forming. Therefore, metallic glass particles are usually preheated to supercooled liquid region in cold spray to achieve better particle bonding and higher deposition efficiency [16–18].

Researchers have studied the formation mechanism of cold sprayed BMG deposits through investigating the deformation behavior of individual particles after high-velocity impact. Yoon et al. [17] classified a deposited Ni-based metallic glass particle into three characteristic regions: “little (or no) deformation” at the north pole of the particle, “shear bands and fracture” at the periphery of the particle, and “melting and viscous flow” features at the bottom, which suggested the generation of strain and temperature gradients in deposited particles. The successful bonding of particles was considered to be related to the viscous flow and melting at the impacting interface, driven by the adiabatic heating [17]. Further, another study pointed out that melting only occurred at the bottom periphery (the fringe of the interface) rather than the entire region as evidenced by the pronounced vein patterns at the bottom of the detached Cu-based metallic glass particle [19]. Henao et al. [20] investigated the homogeneous deformation of individual Zr-based metallic glass particles with finite element method, which used the viscoplastic equations based on free-volume constitutive theory. Their study revealed that the non-Newtonian behavior (shear shinning) promoted the extensive viscoplastic deformation of metallic glass particles, and the homogeneous deformation, including both non-Newtonian and Newtonian flow, promoted the lateral viscous flow of metallic glass particles. The high temperature at the impacting interface allowed the particle to bond with the substrate by metallurgical bonding. These two factors resulted in the formation of cold sprayed BMG deposits [20]. To sum up, the major contribution of the aforementioned studies is that they successfully revealed the important role of impact velocity and impact temperature in the deposition of cold sprayed metallic glass particles and concluded that melting and viscous flow were critical to the bonding of metallic glass particles. However, these studies did not clearly identify and demonstrate the exact bonding location at the interparticle interface via experiment, and failed to explain why some metallic glass particles rebounded after impact. Moreover, all the relevant studies attributed the particle bonding mechanism to the adiabatic-heating-induced melting and viscous flow. Nevertheless, in our experiments, we found another important mechanism that also contributed to the bonding of cold sprayed metallic glass particles, which has never been reported in previous studies. Given these, the first motivation of this work is hence to introduce our new findings associated with the bonding mechanism of cold sprayed metallic glass particles.

Metallic glasses are thermodynamically metastable and tend to transform into their crystalline counterparts when supplied with sufficient energy to overcome the activation barriers associated with the nucleation and growth, e.g., through external stimuli such as mechanical deformation [21–23], thermal annealing [24,25], and electron irradiation [26]. For cold spray, nano-sized crystals were observed at the interface of the deposited Cu-based metallic glass particle, and the area of these nanocrystalline phases increased with the increase of gas pressure [27]. On this basis, it is concluded that the nanocrystallization was associated with the abnormally increased strain at the highly deformed region, which was determined by the kinetic energy of particles upon impact. Although the study has attempted to interpret the crystallization behavior of metallic particles during cold spray, the role of temperature, strain and strain rate in the nanocrystallization event requires to be explored in great detail. Most importantly, the existing studies did not interpret how amorphous structure dynamically evolved into nanocrystals during cold spray deposition (i.e., crystallization mechanism). A good understanding of these two facts is rather critical to fully unlock the microstructure evolution of metallic glass particles during cold spray additive manufacturing process, and this is the second motivation of this work.

2. Material and methodology

2.1. Feedstock material

The $Zr_{55}Cu_{30}Ni_5Al_{10}$ (at%, hereafter referred to as Zr55) amorphous powder produced by high-pressure inert gas atomization was used as feedstock for cold spray due to its good glass forming ability. Fig. 1a and b show the surface morphology of the as-atomized Zr55 amorphous powder characterized by scanning electron microscope (SEM, Carl Zeiss ULTRA Plus, Germany). The majority of the feedstock particles are highly spherical with smooth surfaces. Some micro-satellite particles were attached on larger powder due to their different condensation rates. The phase structure of the Zr55 feedstock powder was analyzed by X-ray diffraction (XRD, Bruker D8, Germany) equipped with Cu-Kα radiation from a range of 2θ values between 20° and 80° (40 kV, 40 mA) at a scanning rate of 1.2° min^{-1}. The XRD spectrum of feedstock powder in Fig. 1c only shows broad diffraction humps, which indicates the powder has an amorphous structure. The size distribution of the powder was measured by a laser diffraction particle analyzer (Mastersizer 2000, Malvern Instruments, UK). As shown in Fig. 1d, the powder has a size range between 5 and 90 μm and a median D10, D50, D90 of 15.68, 32.91 and 58.65 μm, respectively.

2.2. Cold spray deposition process

The deposition of Zr55 was achieved by using an in-house cold spray system (Trinity College Dublin, Ireland) which is composed of high-pressure gas cylinders, gas heater, powder feeder, CNC working platform, de-Laval nozzle and computer control module. The de-Laval nozzle has a round cross-sectional shape with a convergent length of 30 mm, a divergent length of 180 mm, an inlet diameter of 10 mm, a throat diameter of 2 mm and an outlet diameter of 6 mm. The nozzle was water-cooled by a jacket in case of nozzle clogging at elevated temperatures. By referring the processing parameters reported in previous studies [19,20,28,29] and considering the maximum capacity of the self-made cold spray system, compressed nitrogen was selected as propelling gas, and the gas pressure and the temperature were maintained constant at 3.0 MPa and 800 °C, respectively. The standoff distance from the exit of de-Laval Nozzle to the target surface was kept at 30 mm. Two experiments, namely full deposit and single splat deposit, were performed to explore the microstructural evolution and the

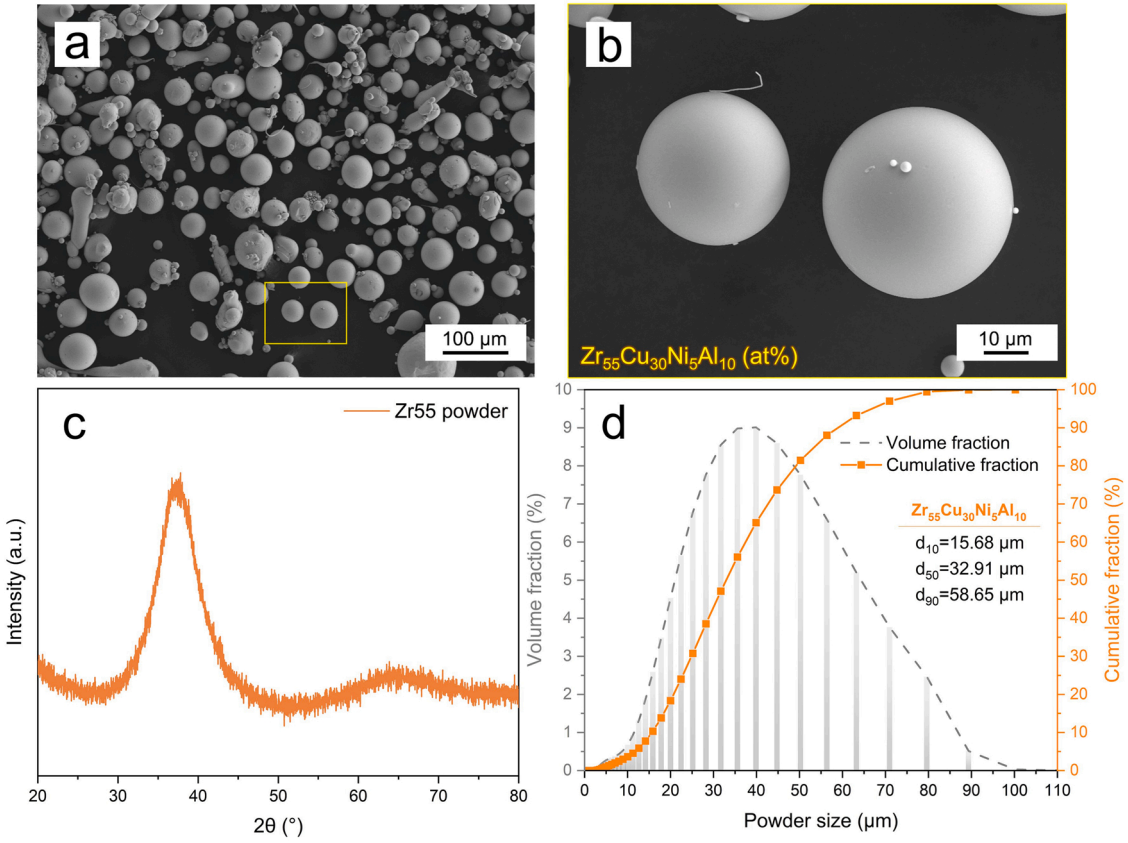

Fig. 1. Characterization of the as-atomized Zr55 amorphous powder used for deposit manufacturing. Surface morphology at (a) low magnification and (b) high magnification, (c) XRD spectrum, (d) particle size distribution.

formation mechanism of the cold sprayed Zr55 deposits. For the full deposit, thick Zr55 deposit was deposited onto Al substrate under a nozzle traversal speed of 50 mm/s and a powder feeding rate of 50 g/min. The nozzle moving trajectory followed a reciprocating zigzag strategy, and the space between two neighboring tracks was 3.0 mm. For the single splat deposit, Zr55 particles were deposited onto mirror-polished cold sprayed Zr55 deposit under a nozzle traversal speed of 150 mm/s and a lower powder feeding rate (10 g/min). The reason for using the as-sprayed Zr55 deposit as substrate material is to simulate the particle-on-particle deposition process during the practical cold spray process.

2.3. Microstructure characterization

As preparatory work for microstructure analysis, the cross-sectional sample was prepared using standard metallographic procedures. In order to reveal the interparticle boundaries, the polished sample was etched with a corrosive agent (a mixture of 15 ml H_2O, 15 ml HNO_3 and 3 ml HF). The microstructure of the cold sprayed Zr55 deposit before and after etching was characterized by SEM. The element compositions of the Zr55 deposit were examined by energy dispersive X-Ray spectroscopy (EDS, Oxford Instruments INCA, UK). The density of the deposit was estimated by optical microscopy (Leica DM LM, Germany) with image analysis method based on ASTM E2109–01 standard. The result was averaged from five different regions of the deposit to ensure the reliability of data. The phase structure of the Zr55 deposit was analyzed by XRD. The micro- and nano-structure at the highly deformed region near the interparticle interface were characterized by transmission electron microscopy (TEM, FEI Tecnai G2 F20) in combination with selected area electron diffraction (SAED). The lamella for TEM characterization was extracted by focused ion beam (FIB, FEI Scios). The fast Fourier transformation (FFT) patterns of the selected regions on TEM images were converted by commercial software (Digital Microscopy, Gatan). Furthermore, the surface and the cross-sectional morphologies of individual Zr55 splats were characterized by SEM, and the cross-sections were prepared through FIB milling.

3. Results and discussion

3.1. General microstructure of the cold sprayed Zr55 deposit

Fig. 2a shows the cross-sectional microstructure of the cold sprayed Zr55 deposit. The deposit is highly dense with few microstructural defects such as pores and cracks. Quantitatively, the density of the deposit was measured to be 99.70 ± 0.13%. The formation of micro-sized pores between some particles can be attributed to the insufficient plastic deformation of particles. In cold spray, a deposit with high density normally suggests that most of the particles experience extensive plastic deformation during deposition and interparticle bonding is promising [14,30]. This is also evidenced by the etched cross-sectional microstructure of the cold sprayed Zr55 deposit shown in Fig. 2c where most of the Zr55 particles were found severely flattened into lamellar shape. However, some of the particles remained spherical or near-spherical due to their insufficient plastic deformation, as pointed out by the yellow arrows in Fig. 2c. The EDS mapping results provided in Fig. 2b indicate that there is no chemical segregation or oxide inclusion in the deposit. This fact indicates the promise of cold spray for manufacturing BMGs with high purity.

Fig. 2d displays the XRD spectrum conducted on the cross-sectional Zr55 deposit. The XRD spectrum shows a broad diffraction peak maximum at around $2\theta = 37°$ without any sharp diffraction peaks as Zr55 feedstock powder, indicating that the deposit retained an

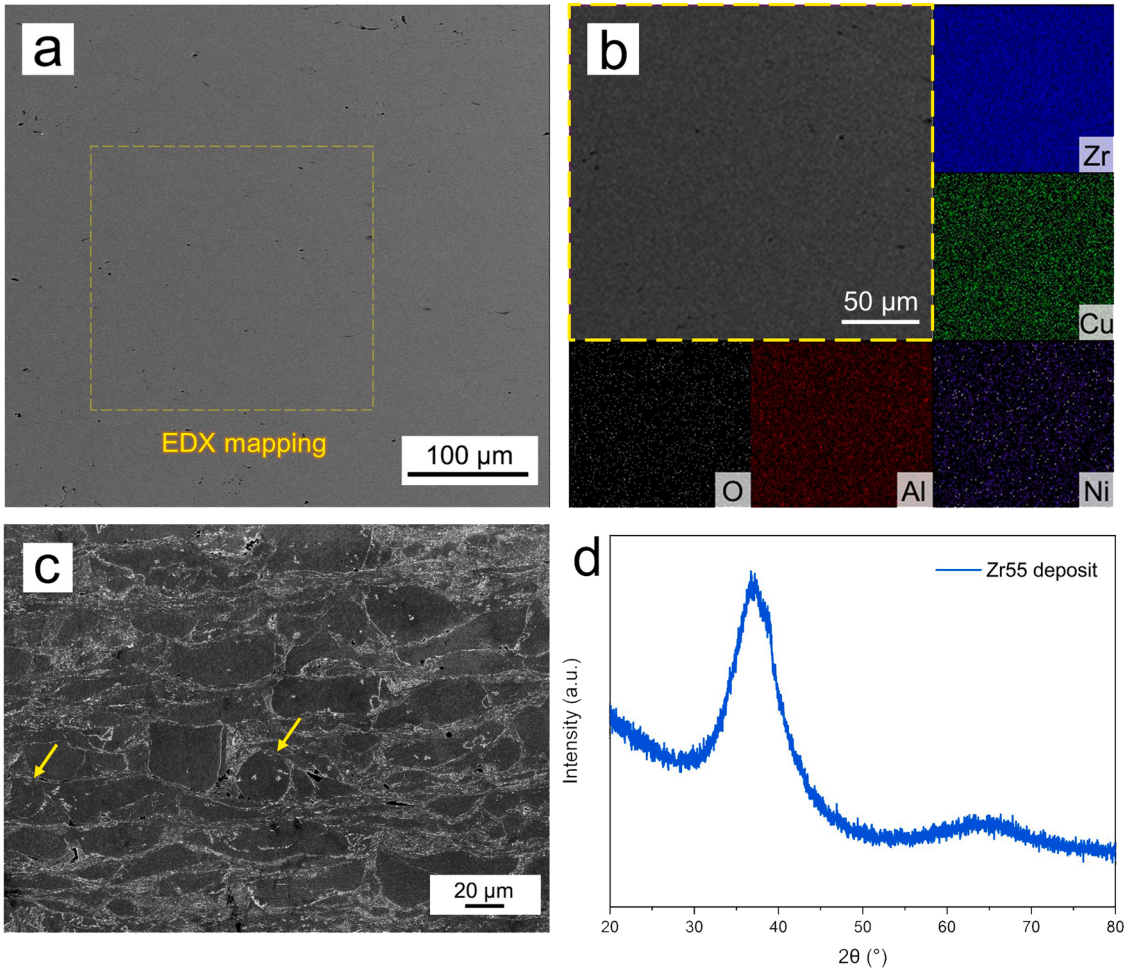

Fig. 2. Characterization of the cold sprayed Zr55 deposit: (a) cross-sectional microstructure, (b) EDS map of elements distribution, (c) etched cross-sectional microstructure, (d) XRD spectrum.

amorphous structure within the detection limit of XRD. This result stands contrast with the XRD spectra of BMGs made by other fusion-based additive manufacturing techniques that often exhibit sharp crystallization peaks [7,31]. Therefore, compared with other additive manufacturing techniques, the inherent characteristics of cold spray such as low temperature, short impacting period, and high cooling rate mitigate the challenge of crystallization during the deposition process. However, it is noteworthy that the deposit may experience nano-crystallization, particularly at the highly deformed impacting interface as previously reported [27].

3.2. Bonding mechanism of individual cold sprayed metallic glass particles

3.2.1. Mechanism I-High-velocity impact induced localized metallurgical bonding at the fringe of the interface

Fig. 3 shows the representative surface morphologies of individual Zr55 particles after impact, and craters created by rebound particles. Fig. 3a shows a deposited particle with high sphericity. It can be seen that shear bands and shear cracks were generated in the particle, which are the typical characteristics of localized flow (inhomogeneous deformation) of metallic glasses. When the particle impacted onto the substrate, the stress at the contact interface increased quickly. Once the stress reached a critical value, yielding occurred and permanent shape change was observed macroscopically through the initiation of shear bands. The shear bands initiated from the bottom of the particle and propagated rapidly towards the north pole with the stress waves travelling the particle. The dominant shear bands finally developed into cracks. At a microscopic level, the formation of shear bands is considered to be associated with the shear transformation zone, in which a group of atoms under imposed shear obtain the stress or strain energy established during elastic loading and overcome the energy barrier by cooperative rearrangement [32]. In addition, thin squeezed material was found at the bottom periphery of the deposited particle, which is the evidence of viscous fluid or melting fluid induced by high temperature and shear strain. Fig. 3b shows a deposited particle with more significant localized flow features (i.e., increased number of shear bands and larger area of shear surface), which could be attributed to the higher kinetic energy of the particle. The shear surface presents vein patterns and white ridge lines at sub-micron scale, indicating the localized softening by adiabatic heating during the rapid shear. Besides, there are some splashing melting (or viscous fluid) jets around the particle as pointed out by the yellow arrow, which suggests the extremely high temperature localized at the bottom of the particle. As shown in Fig. 3c, the particle experienced more severe localized plastic deformation and deformed to a propeller-like shape with further increased area of shear surface. In addition, the shear surface presents flat and smooth appearance, which is quite different from that in Fig. 3b. This could be attributed to the extremely adiabatic temperature during shear banding at higher strain rates, and the temperature within the shear bands may reach the melting point T_m (1028 K [33]). It is reported that the temperature rise associated with shear banding in metallic glass can reach up to a few thousand kelvin over a few nanoseconds [34]. Such high temperature led to the sharply decreased viscosity and thus the smooth shear surface appeared.

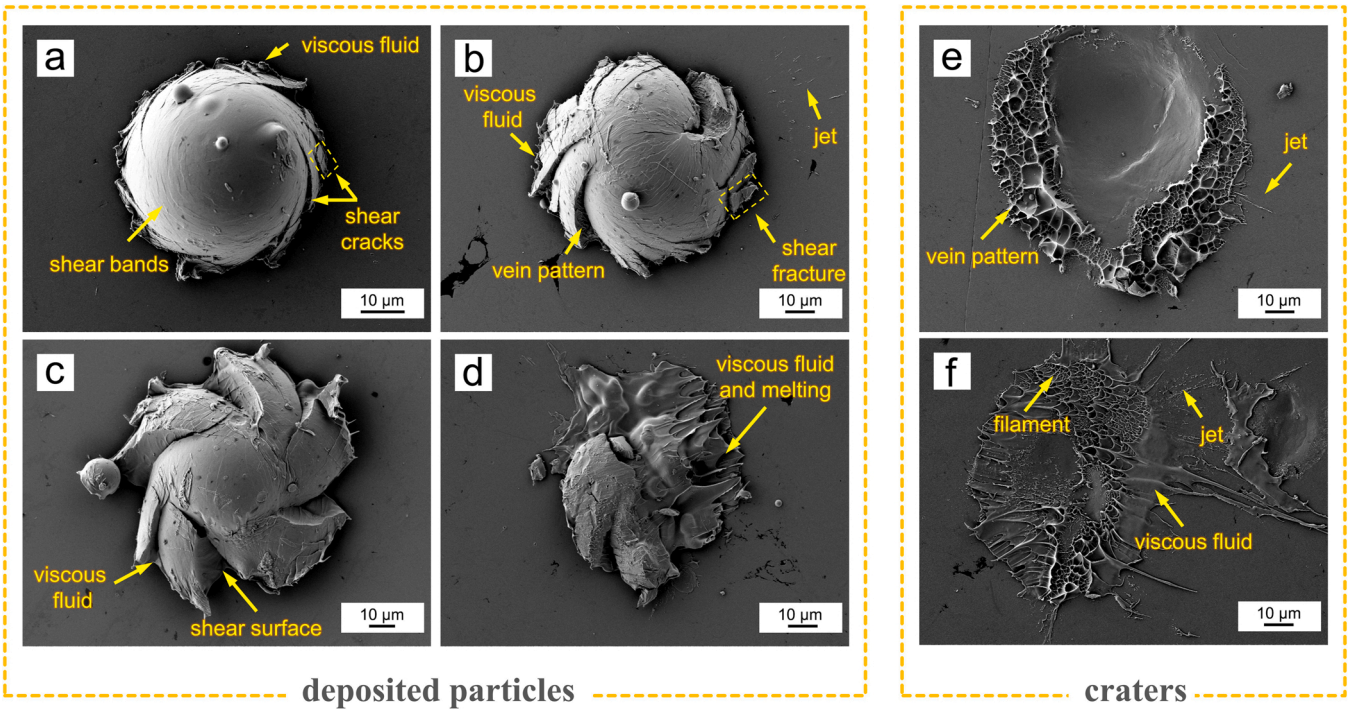

Fig. 3. Top view of the representative surface morphologies of (a)-(d) individual Zr55 deposited particles and (e)-(f) craters created by rebound Zr55 particles. Note the substrate used in single particle deposition is the polished cold-sprayed Zr55 deposit.

Fig. 3d shows a deposited particle with its right part fractured and ejected after impact due to severe shear localization, which provides an opportunity to directly observe what happened at the bottom of the particle. A large volume of viscous fluid or melting fluid can be observed at the bottom region of the particle due to the adiabatic heating induced by highly localized plastic deformation upon impact. Accordingly, there is a reasonable prospect that the localized viscous fluid or melting fluid induced by high temperature occurred at the south pole of the deposited particle, resulting in the particle adhesion to the substrate. The viscous fluid or melting fluid is the strong evidence of homogeneous deformation of the metallic glass particle. The various impact morphologies of the particles shown in Fig. 3a-d can be attributed to their different impact velocities and impact temperatures induced by particle size effect during acceleration. For each single particle, the different deformation features presented from the bottom to the top of the particle is due to the generation of strain gradient, strain rate gradient and temperature gradient upon impact.

Fig. 3e-f show craters on the substrate surface created by rebound Zr55 particles. As shown in Fig. 3e, the central region of the crater is rather clean with nearly no evidence of metallurgical bonding between the particle and the substrate. However, a ring of dimple-like structure (vein pattern as marked by yellow arrows) can be observed at the surrounding area of the crater together with some "melting fluid jets" (or viscous fluid jets). These dimple-like features and viscous jets are the result of the high temperature at the impacting interface. The increased temperature led to the sharp decrease of viscosity, which promoted viscous flow at the bottom periphery of the particle. Actually, the most interesting finding from Fig. 3e-f is that these dimple-like materials remained bonded with the substrate after particle rebounding. The detachment occurred in the particle rather than from the particle-substrate interface. This fact indicates that Zr55 particle can bond with the substrate upon impact in the first place. However, the viscous force of the liquefied interface failed to surpass the particle rebounding force, thus the particle rebounded from the substrate after impact. Therefore, it can be inferred that the successful bonding requires adequate viscous force generated by dimple-like materials between substrate and Zr55 particle.

In order to observe what had happened at the interface exactly and how the metallic glass particles bonded with the previously deposited layer, a deposited Zr55 particle was dug from the top with FIB to display the entire particle-substrate interface. Fig. 4 exhibits the surface morphology of a particle after impact and corresponding cross-sectional morphology including the particle-substrate interface. As shown in Fig. 4a, the deposited particle is characterized by severe shear localization which is the feature of inhomogeneous deformation, representing the common deposition morphology of Zr55 particles. Fig. 4b-c show the cross-sectional morphology of the deposited particle. There is a nanoscale gap between the deposited particle and the substrate except at the fringe of the interface at which the particle bonded with the substrate. The formation of the nanoscale gap can be attributed to the spring back elastic forces. The bonding only occurred at the fringe of the particle-substrate interface, which is consistent with what we see in the crater (see Fig. 3e**)**. This is the first time that the exact bonding location of metallic glass particles was observed experimentally.

3.2.2. Mechanism II- High particle temperature induced viscosity reduction and resultant annular metallurgical bonding band

The outer layers of all the deposited particles in Fig. 3 exhibit the same surface status as feedstock without any trace of viscous fluid or melting fluid, which implies that the surface temperature of these particles was relatively low before impacting. However, the deposited particle, as shown in Fig. 5a, presents an exceptional status where the outer layer of the particle was viscous-flowing. This is probably because the temperature of the outer layer of the particle is much higher (e.g., typically in or above supercooled liquid region) when impacting onto the substrate. The viscosity of metallic glasses is temperature sensitivity and decreases with the increase of temperature. Similar to preheating particles, higher temperature favors particle global deformation and bonding. The bonding mechanism of such particle is associated with the liquid-like outer layer of the particle.

Fig. 5b shows the surface morphology of a deposited particle with liquid-like surface. Compared with the particles in Fig. 4, there are no

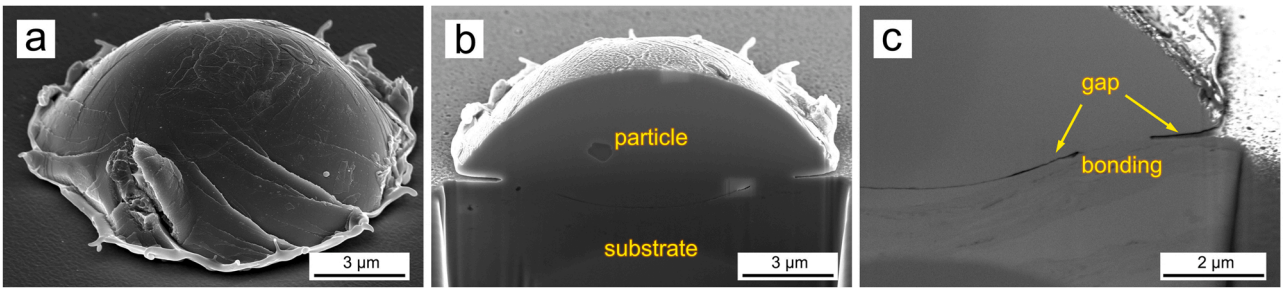

Fig. 4. FIB process of an individual Zr55 deposited particle: (a) surface morphology, (b) cross-sectional morphology revealing the particle-substrate interface, (c) close view of metallurgical bonding at the interface.

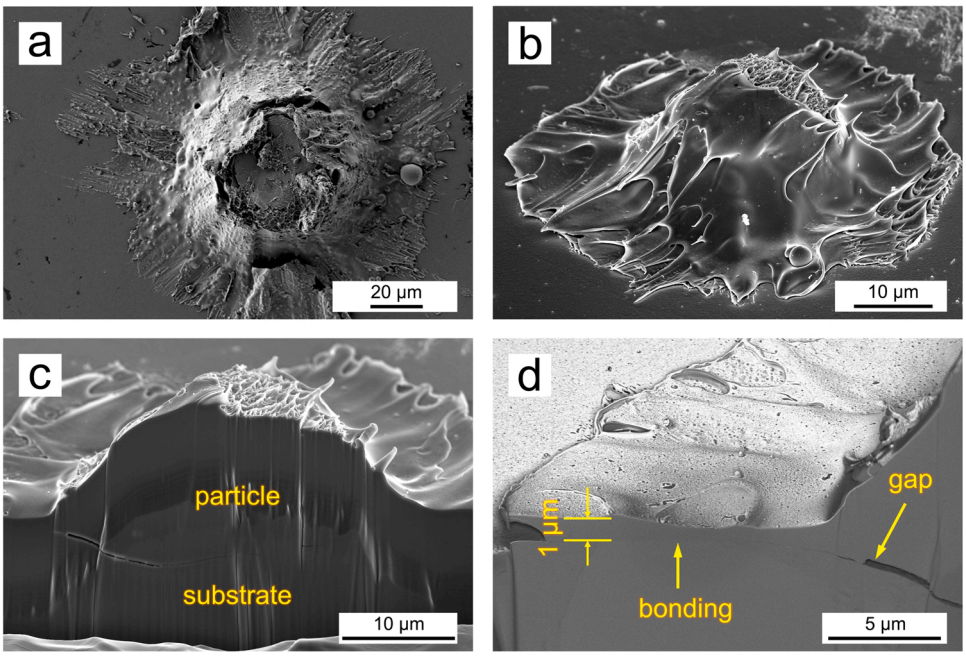

Fig. 5. (a) Top view of the surface morphology of an individual Zr55 deposited particle with liquid-like surface, (b)-(d) FIB process of an individual particle with liquid-like surface: (b) surface morphology, (c) cross-sectional morphology revealing the particle-substrate interface, (d) close view of metallurgical bonding at the interface.

visible shear bands, cracks or fractures, indicating the particle mainly experienced homogeneous deformation. Fig. 5c-d show the cross-sectional morphology of the deposited particle. Discontinuous gap between the particle and the substrate was found at the highly deformed region. However, the close view at the side of the interface shows an annular metallurgical bonding band with a thickness of ~1 μm, which is quite different from the bonding location in Fig. 4c. When the particle impacted onto the substrate at a temperature in or above supercooled liquid region, the viscous fluid was forced to flow to the periphery. The shear thinning induced by high shear rate at the bottom of the particle can further promote the lateral viscous flow of the particle. The viscous fluid at the side of the interface adhered with the substrate through metallurgical bonding promoted by high temperature. In cold spray, particle impact velocities and impact temperatures are affected by many factors, such as particle size and in-flight trajectory. In general, large-sized particles are likely to experience high temperature due to their longer residence. Moreover, particles travelling through the centre of the nozzle experience higher gas temperature, compared with those particles travelling near the inner wall of the nozzle. In brief, some particles probably impacted onto the substrate at temperatures in or above supercooled liquid region. The viscous fluid was forced to flow to the periphery upon impact, and adhered with the substrate through an annular metallurgical bonding band, which is different from the impact induced localized metallurgical bonding.

3.2.3. A summary of the bonding mechanism of cold sprayed metallic glass particles

Based on the results and discussion presented above, it is sensible to conclude that the bonding of the cold sprayed Zr55 particles can be achieved through two different mechanisms. For most of the deposited particles, the bonding was realized by the high-velocity impact induced localized metallurgical bonding at the fringe of the interface. The rising temperature at the impacting interface led to the sharp decrease of viscosity, and promoted lateral homogeneous deformation at the bottom of the metallic glass particle. However, particles will rebound from the substrate if the impact velocities of particles are high enough. Apart from this, an unusual particle bonding mechanism that has never been reported was also found to contribute to the deposition of metallic glass particles. Some particles impacted onto the substrate at temperatures in or above supercooled liquid region, leading to the decrease of viscosity. Upon impact, the viscous fluid was forced to flow to periphery and adhered with the substrate through an annular metallurgical bonding band. The high impact temperature of a particle is related to the particle size and the in-flight trajectory. Specifically, a particle with larger size or travelling through the center of the nozzle is more likely to experience high temperature due to longer residence or higher gas temperature.

Both two particle bonding modes contribute to the formation of the cold sprayed Zr55 deposit.

3.3. Nanocrystallization of cold sprayed metallic glass particles

Fig. 6a shows the interface between two metallic glass particles in the cold sprayed Zr55 deposit observed by SEM. The lamella containing the interparticle interface, as shown in Fig. 6b, was then lifted out by FIB. The nanostructure of two regions S1 (away from the interparticle interface) and S2 (near the interparticle interface) in Fig. 6c was investigated by TEM. Fig. 6d shows the TEM image and corresponding SAED pattern of a region in S1. The diffusion halo in SAED pattern indicates that a glass structure in amorphous phase was well-retained at the region away from the interparticle interface. However, it is interesting to find that a heterogeneous nanostructure with nano-scale dark polygon areas randomly dispersed in the amorphous matrix was observed at the extremely localized near-interface region (S2), as shown in Fig. 6e. The corresponding SAED pattern displays diffuse halo rings with few irregular bright specks, suggesting the coexistence of amorphous and nanocrystal structures. These nanocrystals with dark polygonal structures were believed to form during the particle deposition.

3.3.1. Nanocrystallization conditions: Thermal and mechanical factors

In cold spray process, adiabatic heating at the impacting interface is unavoidable during the high-strain-rate deformation of particles, which leads to considerable temperature rise and material softening. The high temperature can reduce the energy barrier of atomic diffusion, and the formation of nanocrystals through the atomic diffusion mechanism of nucleation and growth in amorphous matrix is possible. In this work, the high temperature can be inferred from the viscous fluid at the bottom of the particles and the metallurgical bonding at the interface (see Fig. 3 and Fig. 4). However, the cooling rate in cold spray process can reach as high as 10^9~10^{10} K·s^{-1} at the highly deformed interfacial regions [35], which is significantly higher than that of gas atomized droplets (10^4~10^6 K·s^{-1} [36,37]). The gas atomized metallic glass powder can retain amorphous structure, so the cooling rate of cold spray is high enough to bypass nanocrystallization. In other words, the effect of adiabatic heating on the formation of nanocrystals at the interparticle interface is considered to be very limited.

In general, the atomic mobility in metallic glasses is frozen when it is cooled below glass transition [38]. However, the plastic deformation is able to assist atomic transportation and evolution toward equilibrium, and thereby lead to the ordering of localized structures. In fact, the nanocrystallization of metallic glasses has been observed in various plastic deformation processes at room or cryogenic temperature, such as rolling [21], nanoindentation [39], high-pressure torsion [40], and ball milling [41], particularly in the region of the deformed specimen under compressive stress. This indicates that the formation of nanocrystals in these low-temperature plastic deformation processes is due to the strain, rather than the deformation induced temperature rise.

Nucleation is a key step in the crystallization process. Crystals can be produced only when the size of nucleation exceeds a critical size. According to classical nucleation theory, the nucleation rate ($\dot{N}$) can be described as [42]:

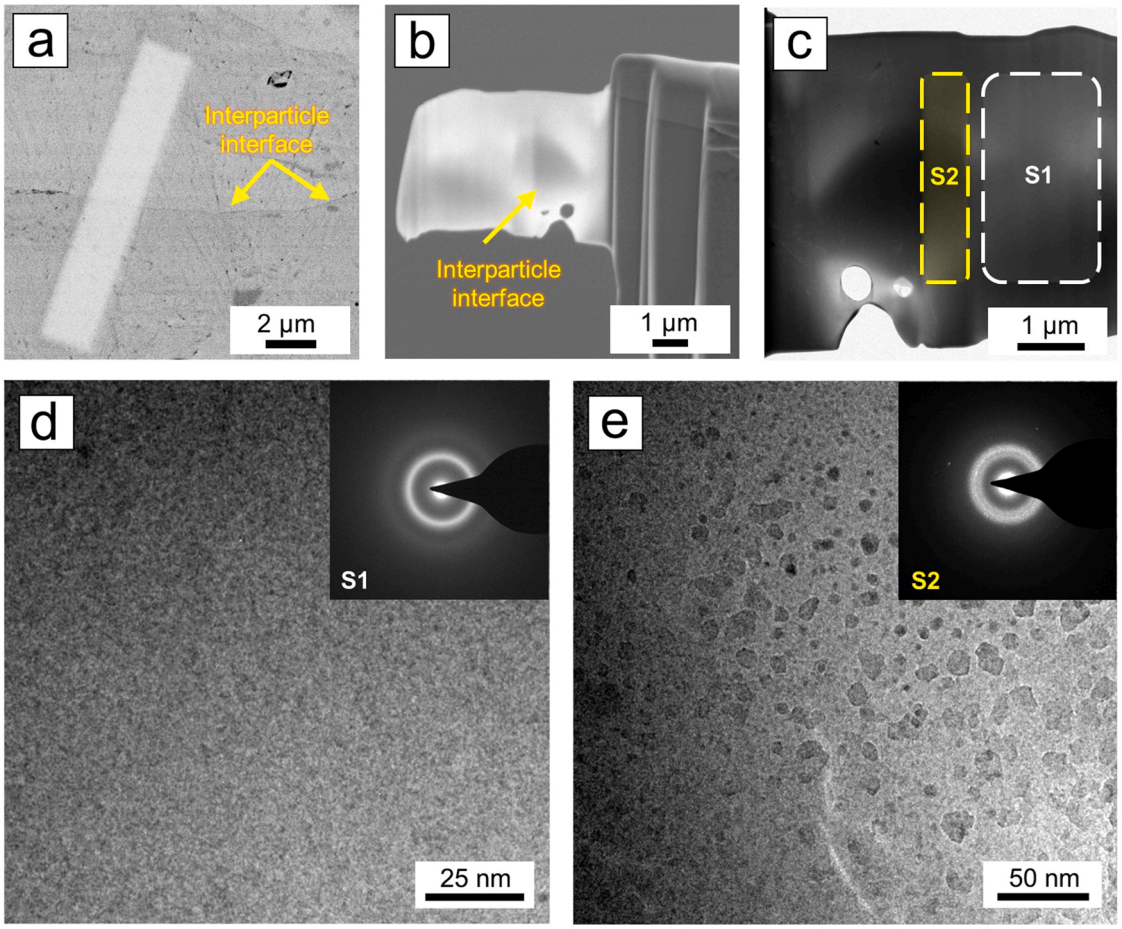

Fig. 6. Characterization of the nanostructure at the interparticle interface: (a) SEM image exhibiting interparticle boundary between two particles, (b) SEM and (c) TEM images of the lamella lifted out by FIB, (d)-(e) TEM micrograph with SAED pattern inset: (d) away from the interparticle interface and (e) near the interparticle interface, respectively.

$$\dot{N} = Nexp(-\frac{\Delta G^*}{kT})exp(-\frac{\Delta E}{kT}) \quad (1)$$

where N is a constant at a fixed temperature, ΔG^* is the energy barrier for nucleation required to form a critical sized nucleus, ΔE is the energy barrier for diffusion required to transport an atom from an amorphous matrix to an embryonic nuclei, k is the Boltzmann's constant. Therefore, the nucleation rate ($\dot{N}$) will increase if the energy barrier for nucleation (ΔG^*) and atomic diffusion (ΔE) are reduced.

The pressure (P) modified energy barrier to form a spherical crystal nucleus with a critical size (ΔG^*) can be expressed as [42]:

$$\Delta G^*(T,P) = \frac{16\pi\gamma^3}{3}(\frac{V_m^c}{\Delta G_m + E + P\Delta V_m})^2 \quad (2)$$

where V_m^c is the molar volume of the crystalline phase, ΔG_m is the molar free energy difference between the amorphous and crystalline phases, E is the elastic energy induced by the volume change during the phase transformation in the solid state, γ is the interfacial free energy between the amorphous and crystalline phases, and ΔV_m is the volume change to form this crystalline nucleus from amorphous state.

During the phase transformation from amorphous to crystalline, the values of ΔG_m and ΔV_m ($\Delta V_m = V_m^c - V_m^a$) are negative and E is rather small [43]. Therefore, the free energy required to produce a critical nucleus size (ΔG^*) decreases with the increasing of pressure. In cold spray, the high pressure at the impacting interface leads to the decreased ΔG^*. Moreover, the crystalline phase possesses smaller volume than that of the amorphous phase, and the crystalline nuclei inlaid in the amorphous matrix are under internal tension. Hence, the applied compressive stress can relieve the tensile stress in the crystalline nuclei and thereby stabilize the crystalline nuclei [44].

Based on the free volume theory, the strain during the plastic deformation of metallic glasses could generate free volume and promote atomic transportation [45–47]. Furthermore, the increase rate of free volume and saturated free-volume content increase with strain rate. Higher strain rate leads to the higher increase rate of free volume and the resultant more free volume generation than lower strain rate. Although the creation of free volume comes along with the annihilation of free volume, the creation rate of free volume at high strain rate exceeds the annihilation rate. Therefore, high strain and high-strain rate deformation could generate more free volume. The increase of free volume leads to atomic dilatation and thereby the reduction in the barrier for mobility of atoms in metallic glasses [48]. In cold spray, the high strain and high strain rate at the impacting interface contribute to the rapid generation of free volume and the rapid transportation of atoms. From the perspective of kinetics, the enhanced atomic transportation can be understood as the decrease of energy barrier for atomic

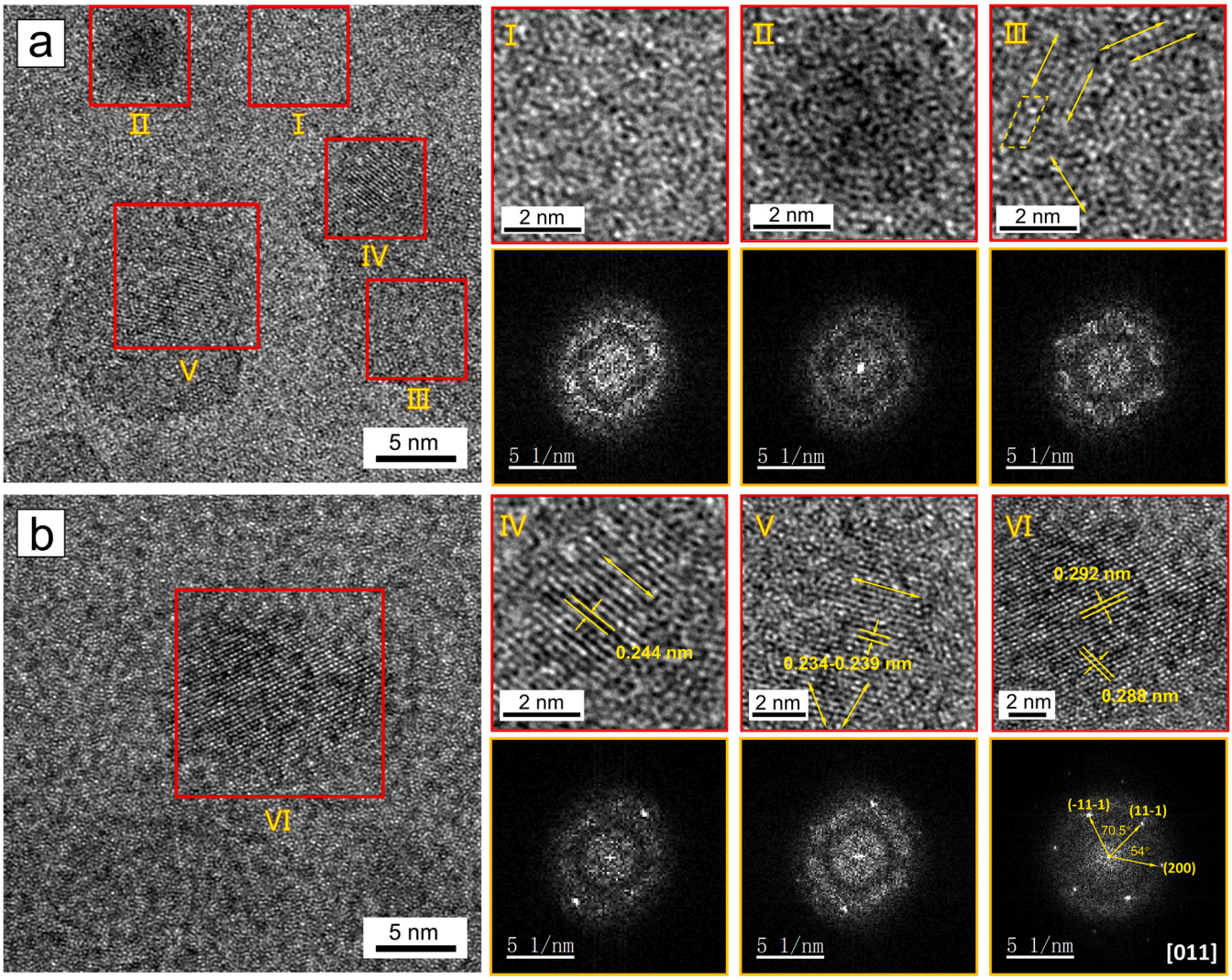

Fig. 7. HRTEM images and corresponding FFT diffraction patterns of localized ordered clusters near the interparticle interface: (a) localized ordered atomic configuration, (b) nanocrystal structure.

diffusion (ΔE). According to Eq. (1), the decreased ΔG^* and ΔE work together to increase the nucleation rate, which promotes the precipitation of nanocrystals from amorphous matrix. Therefore, the effect of mechanical factors on the nanocrystallization in cold sprayed metallic glasses may be decisive.

3.3.2. Nanocrystallization process: From amorphous structure to nanocrystals

In order to investigate how amorphous structure dynamically evolved into nanocrystals during cold spray, high resolution transmission electron microscopy (HRTEM) and corresponding FFT patterns of localized dark regions were achieved as shown in Fig. 7. As a benchmark, the FFT pattern of the amorphous matrix (region I) is provided in the figure as well. Before starting the discussion, it is worth pointing out that in this work we for the first time observed different amorphous/nanocrystal structures in cold sprayed metallic glass particles, which are believed to represent different evolution stages in nanocrystallization process, and this helps us to fully reveal the nanocrystallization mechanism of metallic glass particles during cold spray. In Fig. 7a, the contrast of region II is darker than that of the amorphous matrix, which may indicate that the atomic arrangement here is special. However, the HRTEM image reveals a disordered atomic structure and its corresponding FFT pattern displays a diffuse halo, which is nearly the same as that of the amorphous matrix (region I). This fact suggests that region II is still in amorphous state. The difference in contrast is likely due to the composition segregation in region II [49]. Such segregation is believed to be induced by high mechanical stress and adiabatic temperature rise generated during the high-velocity impact of particles, resulting in the formation of a large amount of free volume and promoting atomic diffusion to accelerate the composition segregation [21,47]. The occurrence of composition segregation is closely related to the interatomic interactions in the alloy. A large difference in the heat of mixing, or a positive heat of mixing between two components can result in phase separation or segregation [50]. In Zr-Cu-Ni-Al alloy system, the Cu and Ni atomic pairs show a positive heat of mixing ($\Delta H_{Cu\text{-}Ni}$ = 4 kJ/mol). The heats of mixing of Zr-Ni ($\Delta H_{Zr\text{-}Ni}$ = −49 kJ/mol) and Zr-Al ($\Delta H_{Zr\text{-}Al}$ = −44 kJ/mol) are more negative than that of other atomic pairs ($\Delta H_{Zr\text{-}Cu}$ = −23 kJ/mol, $\Delta H_{Ni\text{-}Al}$ = −22 kJ/mol and $\Delta H_{Cu\text{-}Al}$ = −1 kJ/mol, respectively) [51]. The strong attractive interaction of Cu-Ni, Zr-Ni and Zr-Al helps the occurrence of segregation in the amorphous matrix.

The atoms in region III show a disordered arrangement which is similar with region I. However, localized ordered atomic lines (or columns) were found in certain directions, as pointed out by the yellow arrows. The clusters in the yellow box are regarded as the feature of imperfect ordered packing [52]. The corresponding FFT diffraction pattern displays a diffuse halo without any bright spots, indicating the entire atomic configuration in this region remains disordered. However, some blurred spots are able to be distinguished. Furthermore, the connection of any two blurred spots, which are symmetry of the central spot, is perpendicular to the corresponding atomic arrangement direction as pointed out in region III. This indicates some atoms started to adjust their position towards an ordered packing. It is more interesting that the ordering process concurrently occurred along multiple directions.

In region IV, the formation of lattice fringes can be clearly observed. The atoms formed highly ordered atomic lines along an exclusive periodic direction through further adjusting their positions. The corresponding FFT diffraction pattern of this atomic configuration shows a diffuse halo together with clearly visible bright specks, indicating the coexistence of amorphous and ordering structure in the current region. In other words, nanocrystallization in this area was incomplete. Moreover, only two bright spots were observed in the FFT pattern, which indicates it has 1D periodic arrangement [53]. Based on the FFT pattern, the 1D periodic arrangement has a plane space of about 0.244 nm, which is the typical (103) plane space of Zr_2Cu. It is worthy to note that the maximum ramp peak of the deposit is located in (103) plane of Zr_2Cu as well. Consequently, it can be inferred that the 1D periodic nanocrystal structure is Zr_2Cu. Furthermore, (103) plane is a relatively low plan index for Zr_2Cu lattice, and the packing of atoms on this plane is denser than that of a plane with higher index. In other words, it is easy for atoms to migrate to a stable site. Therefore, a cluster of single direction atomic columns (1D periodicity) was firstly formed along the low index or close packed direction. Such quasi-ordered structure with 1D periodicity has also been reported in the nanocrystallization of other metallic glasses or even proteins, which was regarded as a primary step to reach a localized equilibrium state [53,54]. Compared with the atoms in region IV, the atoms in region V also exhibit the feature of 1D periodicity. However, localized ordered atomic lines were also formed in other directions. The corresponding FFT diffraction pattern also supports what we observed. Aside from two bright specks indicating the 1D periodicity, other spots with lower brightness were also found. The connection of any two blurred spots, which are symmetry of the central spot, is perpendicular to the corresponding localized ordered direction as pointed out in region V. It can be inferred that the atoms continued to adjust their positions towards a higher-ordered atomic configuration (i.e., 2D or 3D periodicity).

In region VI, as shown in Fig. 7b, almost all the atoms exist in a highly ordered arrangement with 3D periodicity, demonstrating a higher level of nanocrystallization. The nanocrystal structure could be $AlZr_3$, $AlCu_2Zr$ or $AlNi_2Zr$ on the [011] zone axis by calibration. The formation of above intermetallic is likely to be associated with the large difference in the heat of mixing of corresponding elements in Zr55 alloy system. Although the arrangement of atoms in region VI was more orderly, crystal defects (e.g., dislocation or vacancy) were still exist in the nanocrystal structure.

3.3.3. Nanocrystallization mechanism of cold sprayed metallic glass particles

Based on the results and discussion above, the nanocrystallization mechanism in the cold sprayed Zr-based BMG deposit can be summarized as below. When the metallic glass particles impacted onto the substrate at high velocity, the localized interfacial regions underwent severe plastic deformation at extremely high strain rates. The composition segregation induced by mechanical and thermal activation was dramatically promoted due to the increased number of free volume and enhanced atomic diffusion, as shown in region II which presents dark and light difference. The segregation acted as a precursor for further nanocrystallization process. The atoms started to adjust their positions to form localized ordered atomic lines towards multiple directions firstly, as shown in region III, followed by the appearance of 1D periodic lattice fringes. The 1D type ordering atomic clusters comprised an array of planes in the same direction, typically along the low index or close packed direction, as shown in region IV. As nanocrystallization proceeded, the 1D periodicity evolved to higher ordered structures through continuous atomic adjustment until the formation of nanocrystals, as shown in Fig. 8. However, due to the short impacting period ($\sim 10^{-8}$ s [55]) and high cooling rates ($10^9 \sim 10^{10}$ K s^{-1} [35]) in cold spray process, the nanocrystallization level was very limited, and consequently, only nano-scale crystals could be formed at localized regions. In fact, similar evolution was also observed during the nanocrystallization of Zr-based metallic glasses induced by high-density pulse-current treatment [53] and annealing [56,57]. Besides, the nanocrystallization process in amorphous Ni investigated by using molecular dynamics simulation method also showed the formation of ordered transition structures (1D and 2D structures) followed by 3D nanocrystals [53,57]. From the point view of thermodynamics, the energy barrier to form 3D nanocrystals directly is much higher than that to form low dimensional ordered transition structures. While from the kinetic aspect, more atomic rearrangement is required to form 3D nanocrystal, as compared to form transition quasi-ordered structures [57]. The evolution process of atomic structure from an amorphous configuration to 3D nanocrystals

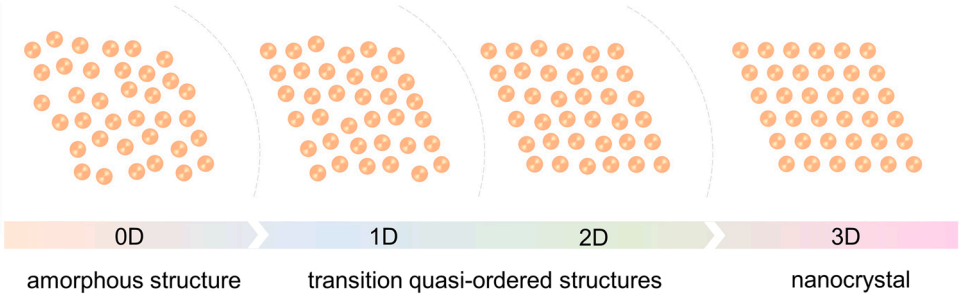

Fig. 8. Schematic of the evolution of nanocrystals from an amorphous state.

is probably universal. Thanks to the nature of cold spray (e.g., extremely rapid heating and cooling rates, short impacting period, and high strain rate), the ordered atomic structures at different stages can be frozen and recorded, which offers us an opportunity to explore the nanocrystallization process of metallic glasses during cold spray process.

4. Conclusions

In this work, the bonding and nanocrystallization mechanisms of cold sprayed metallic glass particles were systematically investigated by using Zr55 metallic glass powder as feedstock. Based on the results and discussion, a number of important conclusions that can significantly enrich our knowledge and understanding of cold sprayed BMG deposits were drawn and listed as follows:

1. For the first time, the exact bonding location of metallic glass particles was observed experimentally. The interparticle bonding only occurred at the fringe area of the interface, which can be attributed to the high-velocity impact induced localized metallurgical bonding.
2. A new mechanism that also contributed to the bonding of cold sprayed metallic glass particles was first found. Some metallic glass particles impacted onto the substrate at temperatures in or above supercooled liquid region, leading to the decrease of viscosity. The viscous fluid was forced to flow to the periphery upon impact, and adhered with the substrate through an annular metallurgical bonding band.
3. Ordered atomic structures at different levels were randomly dispersed in the amorphous matrix near the interparticle interface. The nanocrystallization at interfacial regions was mainly induced by mechanical factors (e.g., high strain and high strain rates) rather than adiabatic heating.
4. The different amorphous/nanocrystal structures in cold sprayed metallic glass particles can represent different evolution stages in the process of nanocrystallization. The formation of nanocrystals from an amorphous state can be divided into following stages: composition segregation, the formation of ordered 1D and 2D transition structures followed by 3D nanocrystals.

CRediT authorship contribution statement

Ningsong Fan: Writing – original draft, Methodology, Investigation, Formal analysis, Data curation. **Chunjie Huang:** Investigation. **Zhongyu Wang:** Formal analysis. **Pengfei Yu:** Formal analysis. **Wen Chen:** Writing – review & editing. **Rocco Lupoi:** Funding acquisition. **Qingge Xie:** Resources. **Lin Liu:** Writing – review & editing, Resources. **Shuo Yin:** Writing – review & editing, Supervision, Formal analysis, Conceptualization.

Declaration of Competing Interest

The authors declare that they have no known competing financial interests or personal relationships that could have appeared to influence the work reported in this paper.

Data Availability

Data will be made available on request.

Acknowledgements

Mr. Ningsong Fan and Dr. Shuo Yin would like to acknowledge the financial support from the China Scholarship Council (CSC) – Trinity College Dublin Joint Scholarship Programme (No. 201906460020) and the fund from the State Key Laboratory of Solidification Processing of China (SKLSP202011). Dr. Chunjie Huang acknowledges the financial support from the Alexander von Humboldt Foundation. Mr. Zhongyu Wang and Mr. Pengfei Yu acknowledge the financial support from the China Scholarship Council. Dr. Wen Chen acknowledges the support from National Science Foundation (CMMI-1927621) and UMass Amherst Faculty Startup Fund. Dr. Lin Liu acknowledges the financial support from the National Natural Science Foundation of China (No. 52061160483). The authors also would like to thank Dr. Aran Rafferty from Trinity College Dublin (TCD) and Advanced Microscopy Laboratory (AML) for the support in data acquisition.

References

[1] W.H. Wang, Bulk metallic glasses with functional physical properties, Adv. Mater. 21 (2009) 4524–4544, https://doi.org/10.1002/adma.200901053.
[2] J.J. Kruzic, Bulk metallic glasses as structural materials: a review, Adv. Eng. Mater. 18 (2016) 1308–1331, https://doi.org/10.1002/adem.201600066.
[3] M.M. Trexler, N.N. Thadhani, Mechanical properties of bulk metallic glasses, Prog. Mater. Sci. 55 (2010) 759–839, https://doi.org/10.1016/j.pmatsci.2010.04.002.
[4] H.R. Lashgari, M. Ferry, S. Li, Additive manufacturing of bulk metallic glasses: fundamental principle, current/future developments and applications, J. Mater. Sci. Technol. 119 (2022) 131–149, https://doi.org/10.1016/j.jmst.2021.09.068.
[5] Y. Li, Y. Shen, M.C. Leu, H.L. Tsai, Building Zr-based metallic glass part on Ti-6Al-4V substrate by laser-foil-printing additive manufacturing, Acta Mater. 144 (2018) 810–821, https://doi.org/10.1016/j.actamat.2017.11.046.
[6] H.Z. Wang, Y.H. Cheng, J.Y. Yang, Q.Q. Wang, Microstructure and properties of laser clad Fe-based amorphous alloy coatings containing Nb powder, J. Non Cryst. Solids 550 (2020), 120351, https://doi.org/10.1016/j.jnoncrysol.2020.120351.
[7] X. Lin, Y. Zhang, G. Yang, X. Gao, Q. Hu, J. Yu, L. Wei, W. Huang, Microstructure and compressive/tensile characteristic of large size Zr-based bulk metallic glass prepared by laser solid forming, J. Mater. Sci. Technol. 35 (2019) 328–335, https://doi.org/10.1016/j.jmst.2018.10.033.
[8] D. Ouyang, N. Li, L. Liu, Structural heterogeneity in 3D printed Zr-based bulk metallic glass by selective laser melting, J. Alloy. Compd. 740 (2018) 603–609, https://doi.org/10.1016/j.jallcom.2018.01.037.
[9] C. Zhang, W. Wang, Y.C. Li, Y.G. Yang, Y. Wu, L. Liu, 3D printing of Fe-based bulk metallic glasses and composites with large dimensions and enhanced toughness by thermal spraying, J. Mater. Chem. A 6 (2018) 6800–6805, https://doi.org/10.1039/c8ta00405f.
[10] G. Wang, Z. Huang, P. Xiao, X. Zhu, Spraying of Fe-based amorphous coating with high corrosion resistance by HVAF, J. Manuf. Process 22 (2016) 34–38, https://doi.org/10.1016/j.jmapro.2016.01.009.
[11] J. Kim, K. Kang, S. Yoon, S. Kumar, H. Na, C. Lee, Oxidation and crystallization mechanisms in plasma-sprayed Cu-based bulk metallic glass coatings, Acta Mater. 58 (2010) 952–962, https://doi.org/10.1016/j.actamat.2009.10.011.
[12] W. Guo, J. Zhang, Y. Wu, S. Hong, Y. Qin, Fabrication and characterization of Fe-based amorphous coatings prepared by high-velocity arc spraying, Mater. Des. 78 (2015) 118–124, https://doi.org/10.1016/j.matdes.2015.04.027.

[13] C. Zhang, D. Ouyang, S. Pauly, L. Liu, 3D printing of bulk metallic glasses, Mater. Sci. Eng. R. Rep. 145 (2021), 100625, https://doi.org/10.1016/j.mser.2021.100625.

[14] S. Yin, P. Cavaliere, B. Aldwell, R. Jenkins, H. Liao, W. Li, R. Lupoi, Cold spray additive manufacturing and repair: Fundamentals and applications, Addit. Manuf. 21 (2018) 628–650, https://doi.org/10.1016/j.addma.2018.04.017.

[15] J. Lu, G. Ravichandran, W.L. Johnson, Deformation behavior of the Zr41.2Ti13.8Cu12.5Ni10Be22.5 bulk metallic glass over a wide range of strain-rates and temperatures, Acta Mater. 51 (2003) 3429–3443, https://doi.org/10.1016/S1359-6454(03)00164-2.

[16] S. Yoon, H.J. Kim, C. Lee, Deposition behavior of bulk amorphous NiTiZrSiSn according to the kinetic and thermal energy levels in the kinetic spraying process, Surf. Coat. Technol. 200 (2006) 6022–6029, https://doi.org/10.1016/j.surfcoat.2005.09.022.

[17] S. Yoon, C. Lee, H. Choi, H. Jo, Kinetic spraying deposition behavior of bulk amorphous NiTiZrSiSn feedstock, Mater. Sci. Eng. A. 415 (2006) 45–52, https://doi.org/10.1016/j.msea.2005.08.132.

[18] S. Yoon, C. Lee, H. Choi, H. Kim, J. Bae, Impacting behavior of bulk metallic glass powder at an abnormally high strain rate during kinetic spraying, Mater. Sci. Eng. A 448–451 (2007) 911–915, https://doi.org/10.1016/j.msea.2006.02.433.

[19] A. List, F. Gärtner, T. Mori, M. Schulze, H. Assadi, S. Kuroda, T. Klassen, Cold spraying of amorphous Cu50Zr50 alloys, J. Therm. Spray. Technol. 24 (2014) 108–118, https://doi.org/10.1007/s11666-014-0187-x.

[20] J. Henao, A. Concustell, S. Dosta, G. Bolelli, I.G. Cano, L. Lusvarghi, J. M. Guilemany, Deposition mechanisms of metallic glass particles by cold gas spraying, Acta Mater. 125 (2017) 327–339, https://doi.org/10.1016/j.actamat.2016.12.007.

[21] Q.P. Cao, J.F. Li, Y.H. Zhou, A. Horsewell, J.Z. Jiang, Effect of rolling deformation on the microstructure of bulk Cu60Zr20Ti20 metallic glass and its crystallization, Acta Mater. 54 (2006) 4373–4383, https://doi.org/10.1016/j.actamat.2006.05.030.

[22] A.J. Kim, Y. Choi, S. Suresh, A.S. Argon, Nanocrystallization during nanoindentation of a bulk amorphous metal alloy at room temperature, Science 295 (80-) (2002) 654–657. Published by: American Association for the Advancement of Science Stable URL: http://www.jstor.org/stable/3075692 Linked references are available on JSTOR for.

[23] S. Shukla, D.T. Wu, H. Ramanarayan, D. Srolovitz, R.V. Ramanujan, Nanocrystallization in driven amorphous materials, Acta Mater. 61 (2013) 3242–3248, https://doi.org/10.1016/j.actamat.2013.02.012.

[24] E. Pekarskaya, J.F. Löffler, W.L. Johnson, Microstructural studies of crystallization of a Zr-based bulk metallic glass, Acta Mater. 51 (2003) 4045–4057, https://doi.org/10.1016/S1359-6454(03)00225-8.

[25] Q. Wang, C.T. Liu, Y. Yang, Y.D. Dong, J. Lu, Atomic-scale structural evolution and stability of supercooled liquid of a Zr-based bulk metallic glass, Phys. Rev. Lett. 106 (2011) 1–4, https://doi.org/10.1103/PhysRevLett.106.215505.

[26] T. Nagase, Y. Umakoshi, Electron irradiation induced crystallization of the amorphous phase in Zr-Cu based metallic glasses with various thermal stability, Mater. Trans. 45 (2004) 13–23, https://doi.org/10.2320/matertrans.45.13.

[27] S. Yoon, G. Bae, Y. Xiong, S. Kumar, K. Kang, J.J. Kim, C. Lee, Strain-enhanced nanocrystallization of a CuNiTiZr bulk metallic glass coating by a kinetic spraying process, Acta Mater. 57 (2009) 6191–6199, https://doi.org/10.1016/j.actamat.2009.08.045.

[28] A. List, F. Gärtner, T. Schmidt, T. Klassen, Impact conditions for cold spraying of hard metallic glasses, J. Therm. Spray. Technol. 21 (2012) 531–540, https://doi.org/10.1007/s11666-012-9750-5.

[29] J. Su, J. Kang, W. Yue, G. Ma, Z. Fu, L. Zhu, D. She, H. Wang, C. Wang, Comparison of tribological behavior of Fe-based metallic glass coatings fabricated by cold spraying and high velocity air fuel spraying, J. Non Cryst. Solids 522 (2019), 119582, https://doi.org/10.1016/j.jnoncrysol.2019.119582.

[30] H. Assadi, H. Kreye, F. Gärtner, T. Klassen, Cold spraying – a materials perspective, Acta Mater. 116 (2016) 382–407, https://doi.org/10.1016/j.actamat.2016.06.034.

[31] D. Ouyang, Q. Zheng, L. Wang, H. Wang, C. Yang, P. Zhang, N. Li, The brittleness of post-treatment of 3D printed Zr-based metallic glasses in supercooled liquid state, Mater. Sci. Eng. A 782 (2020), 139259, https://doi.org/10.1016/j.msea.2020.139259.

[32] A.L. Greer, Y.Q. Cheng, E. Ma, Shear bands in metallic glasses, Mater. Sci. Eng. R. Rep. 74 (2013) 71–132, https://doi.org/10.1016/j.mser.2013.04.001.

[33] O. Haruyama, Y. Nakayama, R. Wada, H. Tokunaga, J. Okada, T. Ishikawa, Y. Yokoyama, Volume and enthalpy relaxation in Zr55Cu30Ni5Al10 bulk metallic glass, Acta Mater. 58 (2010) 1829–1836, https://doi.org/10.1016/j.actamat.2009.11.025.

[34] J.J. Lewandowski, A.L. Greer, Temperature rise at shear bands in metallic glasses, Nat. Mater. 5 (2006) 15–18, https://doi.org/10.1038/nmat1536.

[35] T. Schmidt, F. Gärtner, H. Assadi, H. Kreye, Development of a generalized parameter window for cold spray deposition, Acta Mater. 54 (2006) 729–742, https://doi.org/10.1016/j.actamat.2005.10.005.

[36] B. Zheng, Y. Lin, Y. Zhou, E.J. Lavernia, Gas atomization of amorphous aluminum: Part I. thermal behavior calculations, Metall. Mater. Trans. B Process. Metall. Mater. Process. Sci. 40 (2009) 768–778, https://doi.org/10.1007/s11663-009-9276-5.

[37] M. Zhang, Z. Zhang, Numerical simulation study on cooling of metal droplet in atomizing gas, Mater. Today Commun. 25 (2020), 101423, https://doi.org/10.1016/j.mtcomm.2020.101423.

[38] Z. Kovács, P. Henits, A.P. Zhilyaev, Á. Révész, Deformation induced primary crystallization in a thermally non-primary crystallizing amorphous Al85Ce8Ni5Co2 alloy, Scr. Mater. 54 (2006) 1733–1737, https://doi.org/10.1016/j.scriptamat.2006.02.004.

[39] J.J. Kim, Y. Choi, S. Suresh, A.S. Argon, Nanocrystallization during nanoindentation of a bulk amorphous metal alloy at room temperature, Science 295 (80-) (2002) 654–657, https://doi.org/10.1126/science.1067453.

[40] S.H. Joo, D.H. Pi, A.D.H. Setyawan, H. Kato, M. Janecek, Y.C. Kim, S. Lee, H. S. Kim, Work-hardening induced tensile ductility of bulk metallic glasses via high-pressure torsion, Sci. Rep. 5 (2015) 1–9, https://doi.org/10.1038/srep09660.

[41] G.J. Fan, M.X. Quan, Z.Q. Hu, W. Löser, J. Eckert, Deformation-induced microstructural changes in Fe 40 Ni 40 P 14 B 6 metallic glass, J. Mater. Res 14 (1999) 3765–3774, https://doi.org/10.1557/JMR.1999.0510.

[42] S.W. Lee, M.Y. Huh, S.W. Chae, J.C. Lee, Mechanism of the deformation-induced nanocrystallization in a Cu-based bulk amorphous alloy under uniaxial compression, Scr. Mater. 54 (2006) 1439–1444, https://doi.org/10.1016/j.scriptamat.2006.01.002.

[43] Y.X. Zhuang, J.Z. Jiang, T.J. Zhou, H. Rasmussen, L. Gerward, M. Mezouar, W. Crichton, A. Inoue, Pressure effects on Al89La6Ni5 amorphous alloy crystallization, Appl. Phys. Lett. 77 (2000) 4133–4135, https://doi.org/10.1063/1.1332409.

[44] S.W. Lee, M.Y. Huh, E. Fleury, J.C. Lee, Crystallization-induced plasticity of Cu-Zr containing bulk amorphous alloys, Acta Mater. 54 (2006) 349–355, https://doi.org/10.1016/j.actamat.2005.09.007.

[45] A. Argon, Plastic deformation in metallic glasses, Acta Met. 27 (1979) 47–58, https://doi.org/10.1016/0001-6160(79)90055-5.

[46] F. Spaepen, A microscopic mechanism for steady state inhomogeneous flow in metallic glasses, Acta Met. 25 (1977) 407–415, https://doi.org/10.1016/0001-6160(77)90232-2.

[47] Q.P. Cao, J.F. Li, Y.H. Zhou, A. Horsewell, J.Z. Jiang, Free-volume evolution and its temperature dependence during rolling of Cu60Zr20Ti20 bulk metallic glass, Appl. Phys. Lett. 87 (2005), 101901, https://doi.org/10.1063/1.2037858.

[48] W.H. Jiang, M. Atzmon, Mechanically-assisted nanocrystallization and defects in amorphous alloys: a high-resolution transmission electron microscopy study, Scr. Mater. 54 (2006) 333–336, https://doi.org/10.1016/j.scriptamat.2005.09.052.

[49] S. Yoon, Y. Xiong, K. Kang, G. Bae, C. Lee, Phase separation in kinetic sprayed bulk metallic glasses, J. Phys. D. Appl. Phys. 42 (2009), 182007, https://doi.org/10.1088/0022-3727/42/18/182007.

[50] B.J. Park, H.J. Chang, D.H. Kim, W.T. Kim, In situ formation of two amorphous phases by liquid phase separation in Y-Ti-Al-Co alloy, Appl. Phys. Lett. 85 (2004) 6353–6355, https://doi.org/10.1063/1.1842360.

[51] A. Takeuchi, A. Inoue, Classification of bulk metallic glasses by atomic size difference, heat of mixing and period of constituent elements and its application to characterization of the main alloying element, Mater. Trans. 46 (2005) 2817–2829, https://doi.org/10.2320/matertrans.46.2817.

[52] G.L. Chen, X.J. Liu, X.D. Hui, H.Y. Hou, K.F. Yao, C.T. Liu, J. Wadsworth, Molecular dynamic simulations and atomic structures of amorphous materials, Appl. Phys. Lett. 88 (2006) 20–23, https://doi.org/10.1063/1.2198015.

[53] X.J. Liu, G.L. Chen, H.Y. Hou, X. Hui, K.F. Yao, Z.P. Lu, C.T. Liu, Atomistic mechanism for nanocrystallization of metallic glasses, Acta Mater. 56 (2008) 2760–2769, https://doi.org/10.1016/j.actamat.2008.02.019.

[54] S.-T. Yau, P.G. Vekilov, Quasi-planar nucleus structure in apoferritin crystallization, Nature 406 (2000) 494–497, https://doi.org/10.1038/35020035.

[55] J. Wu, H. Fang, H.J. Kim, C. Lee, High speed impact behaviors of Al alloy particle onto mild steel substrate during kinetic deposition, Mater. Sci. Eng. A. 417 (2006) 114–119, https://doi.org/10.1016/j.msea.2005.11.011.

[56] X.J. Liu, X.D. Hui, G.L. Chen, M.H. Sun, In situ synchrotron SAXS study of nanocrystallization in Zr65Ni25Ti10 metallic glass, Intermetallics 16 (2008) 10–15, https://doi.org/10.1016/j.intermet.2007.06.014.

[57] X.J. Liu, G.L. Chen, F. Li, X.D. Hui, Z.P. Lu, F. Ye, C.T. Liu, Evolution of atomic ordering in metallic glasses, Intermetallics 18 (2010) 2333–2337, https://doi.org/10.1016/j.intermet.2010.08.004.